Research Article Vol. 34, No. 18 / 7 Sep 2026 / Optics Express 33292

Optics EXPRESS

Microporous diffractive filter for infrared rejection in high-harmonic generation setups

FRANCESCO CORAZZA,[1,4] EMMANOUIL KECHAOGLOU,[1] AIMEE J. ROSS,[2] PETER SMORENBURG,[2] CARL S. LEHMANN,[1] DAVID P. O'DWYER,[2] AND PETER M. KRAUS[1,3,5]

[1] *Advanced Research Center for Nanolithography, Science Park 106, 1098 XG Amsterdam, The Netherlands*
[2] *ASML Research, ASML Netherlands B.V., 5504 DR Veldhoven, The Netherlands*
[3] *LaserLaB, Department of Physics and Astronomy, Vrije Universiteit, De Boelelaan 1105, 1081 HV Amsterdam, The Netherlands*
[4] *corazza@arcnl.nl*
[5] *kraus@arcnl.nl*

Abstract: High-harmonic-generation beamlines require efficient suppression of the co-propagating infrared driver while transmitting broadband short-wavelength radiation. Existing solutions rely on absorption or reflection and are limited by bandwidth, angular constraints, and low damage thresholds. We demonstrate microporous filters as transmissive diffractive elements that suppress infrared by redistributing it into off-axis diffraction orders while preserving short-wavelength transmission. A scalar diffraction model links open-area ratio to transmission. Experiments show on-axis infrared suppression down to 1.1% while transmitting broadband short-wavelength radiation over the 8–19 nm range. Microporous filters withstand average intensities up to 160 W/cm^2 without degradation, yielding $>10\times$ spectral purity improvement and enabling power scaling in high-harmonic-generation beamlines.

1. Introduction

High-order harmonic generation (HHG) has become a key table-top technology for producing coherent extreme ultraviolet [1] (XUV) and soft X-ray [2] (SXR) radiation for applications ranging from attosecond science [3], and ultrafast soft-X-ray spectroscopy [4] to advanced metrology and materials science [5,6]. In HHG sources, the generated short-wavelength radiation co-propagates with an intense infrared (IR) or near-infrared (NIR) driving laser, whose residual power exceeds that of the XUV by several orders of magnitude. The suppression of the driving field is therefore essential to protect downstream optics, samples, and detectors, and to reduce the impact of long-wavelength radiation on background signals. As HHG sources move toward higher average power [7] and larger pulse energies to pursue improved XUV/SXR flux [8,9] and extended spectral coverage [10], effective solutions are required to manage thermal load and ensure long-term stability.

Several approaches have been developed to suppress the residual IR radiation while transmitting XUV/SXR light. Thin metallic filters [11] are widely used because of their simplicity, but they suffer from intrinsic bandwidth limitations, mechanical fragility, oxidation, and performance degradation under high thermal load. Grazing-incidence plates and Brewster-angle beam splitters [12,13] offer higher damage thresholds, yet introduce strong angular sensitivity and typically operate efficiently only over limited spectral ranges. Multilayer mirrors [14,15] provide wavelength selectivity, albeit with narrow bandwidth and increased system complexity. Diffraction gratings [16,17] efficiently separate XUV/SXR from IR radiation, but are costly, require grazing-incidence configurations with a substantial spatial footprint and still have a limited bandwidth. A complementary, source-side approach is to drive HHG with an annular beam [18]. The harmonics emitted along the propagation axis exhibit a smaller divergence than

#608226 https://doi.org/10.1364/OE.608226
Journal © 2026 Received 11 Jun 2026; revised 28 Jul 2026; accepted 12 Aug 2026; published 26 Aug 2026

the driving field, so that the residual IR can be blocked by a simple aperture in the far field. A few studies have reported on the effectiveness of IR rejection [19] and on the impact on the phase-matching conditions [20] of this generation geometry. While effective, annular-beam HHG modifies the geometry of the source itself and it only alleviates the thermal-load problem at the downstream filters at the cost of generation efficiency. As a result, no established solution simultaneously combines broadband transmission, strong IR suppression, and robustness against thermal loads.

Diffractive filters based on periodic microstructures provide an alternative approach by exploiting the strong wavelength dependence of diffraction rather than absorption or reflection [21–23]. Microchannel plates (MCPs), for example, can efficiently diffract long-wavelength radiation out of the optical axis while transmitting short-wavelength radiation predominantly in the zeroth diffraction order [24,25]. This principle enables intrinsically broadband operation combined with high damage tolerance and material robustness, which are attractive features for high-power HHG environments. More generally, transmissive microporous structures can be regarded as engineered diffractive elements whose geometry directly determines the IR suppression along the XUV beam path and short-wavelength transmission. In this context, a quantitative experimental assessment of microporous diffractive filters, spanning IR suppression and XUV transmission, is required to evaluate their suitability for power-scaled HHG sources.

In this work, we demonstrate the use of microporous filters (MPFs) as broadband diffractive elements for IR suppression in XUV/SXR beamlines. Rather than replacing existing IR rejection schemes, MPFs are conceived as an additional compact filtering stage, redirecting residual IR into off-axis diffraction orders and easing the thermal load on the downstream optics. We first describe the design principles, fabrication, and characterization of MPFs with different geometries and open-area ratios. We then introduce an analytical diffraction model that links filter geometry to wavelength-dependent transmission. Next, we experimentally quantify IR rejection and compare the results with model predictions. Finally, we investigate MPF transmission in the XUV domain, demonstrating broadband behavior and assessing suitability for power scaling in HHG applications.

2. Methods

2.1. Microporous filter design and fabrication

MPFs were designed as transmissive diffractive elements that operate in vacuum conditions along the laser beam-path. These devices (see Fig. 1) were fabricated on Silicon-on-insulator wafers coated with a 200 nm thick metallic (Au) layer, using Deep Ultraviolet (DUV) lithography, combined with etching steps including wet etching and Deep Reactive Ion Etching (DRIE) [26,27]. The front side metallic coating was designed to improve the reflectivity and thermal conductivity of the structure. The finished devices consist of disks 0.525 mm thick with 25 mm diameters, with a patterned area at their center 10 μm thick with a diameter of 10 mm. The core of an MPF is a microstructure composed of a silicon membrane patterned with an array of hollow through-channels arranged to follow a bi-dimensional periodicity. Two lattice geometries were investigated: square and hexagonal (honeycomb). For each geometry, filters with different open-area ratios (OAR) were fabricated to systematically study the trade-off between XUV transmission and IR diffraction efficiency. In this context, the OAR is defined as the fraction of the membrane surface occupied by the channel apertures. The membrane thickness was chosen such that the structure behaves as a thin binary diffraction grating. The resulting low aspect ratio of the apertures ensures minimal beam clipping and relaxed angular alignment tolerances with respect to the laser beam path, especially when compared to MCPs with long, high-aspect-ratio channels.

The open-area ratio of each MPF was quantified using optical microscopy combined with image processing. Bright-field images of representative regions were acquired with 20x magnification

Optics EXPRESS

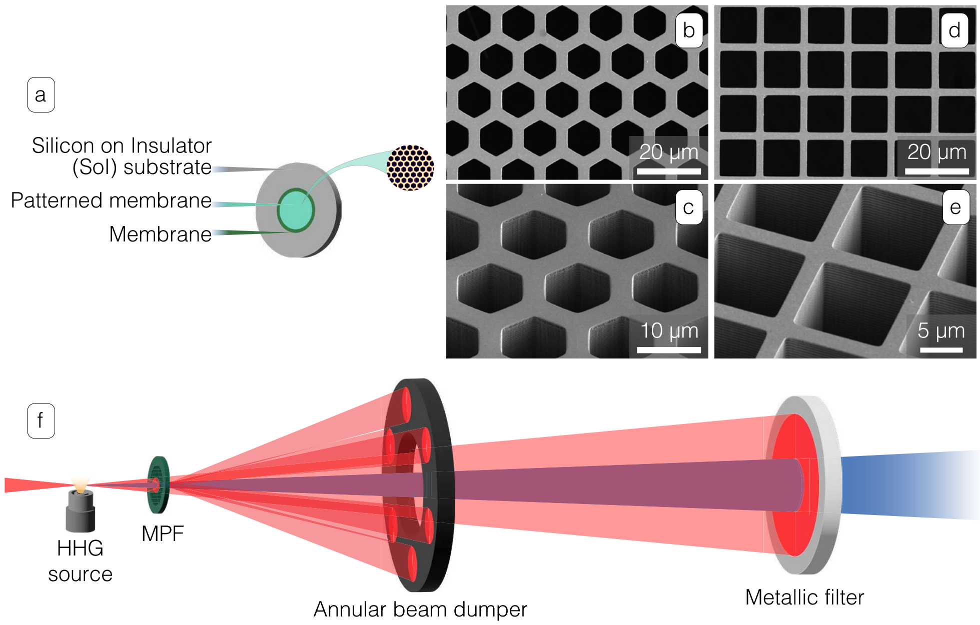

Fig. 1. a) Schematic representation of a microporous filter (MPF). b,c) SEM imaging of MPF with honeycomb lattice, with no tilt in b), and with 45° tilt in c). d,e) SEM imaging of MPF with square lattice, with no tilt in d), and with 45° tilt in e). f) Schematic representation of a MPF device and layout of the implementation of MPFs in an infrared filtering apparatus for high-harmonic generation sources.

objective and analyzed using an active threshold discriminator to distinguish the apertures of the channels from the supporting membrane. The OAR was calculated as the ratio between the number of pixels classified as open and the total number of pixels within the analyzed area. We have characterized the OAR of both sides of each MPF to ensure consistency of the through-channels. The OAR characterization was validated by cross-checking against off-focus flux quantification measurements and iterating the same procedure described above using Scanning Electron Microscopy (SEM). For all samples, the absolute uncertainty in the extracted OAR was below 1%.

The work hereby presented reports results obtained with 6 different MPFs, all with a pitch of 14.0 μm, 3 with square lattice and 3 with honeycomb lattice. The structures of these two sets were fabricated aiming to OARs of 25%, 60% and 75%. The actual OAR obtained after fabrication and corresponding channel sized are reported in Table 1.

2.2. Diffraction model

The diffractive behavior of the MPFs was described using a scalar diffraction model based on the Fraunhofer approximation [28].

MPFs are here modeled for the square lattice geometry. We assume to have a thin binary amplitude grating, an approximation justified by the low aspect ratio of the through-channels relative to the membrane thickness. The two-dimensional transmission function is $T(x, y) = T_x(x)\, T_y(y)$, where each factor is a periodic rectangular function with period p and open aperture L. In this context, the open-area ratio is $\mathrm{OAR} = (L/p)^2$.

Table 1. Nominal and measured open-area ratios (OAR) and channel sizes of the six microporous filters used in this work. All devices share a pitch of p = 14.0 μm, and the characterization reports the 3σ uncertainties. In the honeycomb lattice case, the channel width is defined as twice the apothem of the hexagonal channels

Sample	Lattice	Nominal OAR	Actual OAR	Channel width (μm)
MPF A	Honeycomb	0.25	0.249 ± 0.003	6.8 ± 0.3
MPF B	Honeycomb	0.60	0.552 ± 0.009	10.3 ± 0.2
MPF C	Honeycomb	0.75	0.662 ± 0.006	11.4 ± 0.3
MPF D	Square	0.25	0.260 ± 0.006	6.9 ± 0.5
MPF E	Square	0.60	0.563 ± 0.009	10.5 ± 0.1
MPF F	Square	0.75	0.667 ± 0.006	11.4 ± 0.5

For a Gaussian incident beam with $1/e$ half-width w_0, the near-field amplitude is:

$$E_n(x,y) = E_0 \exp\left[-\frac{x^2}{w_0^2}\right] \exp\left[-\frac{y^2}{w_0^2}\right] \tag{1}$$

In the Fraunhofer regime, the far-field amplitude is given by the two-dimensional Fourier transform of the product of the incident field and the transmission function:

$$E_f(\theta_x,\theta_y) \propto \mathcal{F}\Big[E_n(x,y)\cdot T(x,y)\Big] = \mathcal{F}\Big[E_n^{(x)}\cdot T_x\Big](\theta_x)\,\mathcal{F}\Big[E_n^{(y)}\cdot T_y\Big](\theta_y) \tag{2}$$

$\mathcal{F}$ denotes the one-dimensional Fourier transform, $E_n^{(x)}(x) = E_0^{1/2}\exp(-x^2/w_0^2)$, and $E_f(\theta_x,\theta_y)$ was factorized into independent one-dimensional transforms thanks to the separability of its terms. By the convolution theorem, each factor equals the convolution of the individual Fourier transforms of $E_n^{(x)}$ and T_x, respectively. It follows that:

$$\mathcal{F}\Big[E_n^{(x)}\cdot T_x\Big](\theta_x) = \mathcal{F}\Big[E_n^{(x)}\Big](\theta_x) * \mathcal{F}\Big[T_x\Big](\theta_x) \tag{3}$$

The Fourier transform of the Gaussian factor is a Gaussian itself:

$$\mathcal{F}\Big[E_n^{(x)}\Big](\theta_x) \propto \exp\left(-\frac{k^2 w_0^2 \theta_x^2}{4}\right) \equiv g(\theta_x) \tag{4}$$

The Fourier transform of the periodic function T_x consists of a discrete comb of delta functions.

$$\mathcal{F}\Big[T_x\Big](\theta_x) = \lambda\left(c_0\,\delta(\theta_x) + \sum_{m=1}^{\infty}\frac{c_m}{2}\left[\delta\left(\theta_x - \frac{m\lambda}{p}\right) + \delta\left(\theta_x + \frac{m\lambda}{p}\right)\right]\right). \tag{5}$$

with coefficients:

$$c_0 = \frac{L}{p}, \qquad c_m = \frac{2L}{p}\,\mathrm{sinc}\left(\frac{mL}{p}\right) \tag{6}$$

Taking the convolution of $g(\theta_x)$ with this comb of delta functions replaces each delta function with a copy of the Gaussian g, yielding a discrete set of Gaussian beams centered at the diffraction angles $\theta_m = \pm m\lambda/p$:

$$\mathcal{F}\Big[E_n^{(x)}\cdot T_x\Big](\theta_x) \propto c_0\,g(\theta_x) + \sum_{m=1}^{\infty}\frac{c_m}{2}\left[g\left(\theta_x - \frac{m\lambda}{p}\right) + g\left(\theta_x + \frac{m\lambda}{p}\right)\right] \tag{7}$$

The same expression holds in the y direction by symmetry. All diffraction orders therefore share the same Gaussian envelope shape, with different amplitudes. These are set by the corresponding Fourier coefficient c_m, and the intensity in each order is proportional to $|c_m|^2$.

Integrating the intensity over all diffraction orders and normalizing it to the incident power, the total transmitted fraction equals the OAR, consistent with energy conservation for a lossless amplitude grating with fully opaque walls. The sum of squared amplitudes of all diffraction orders equals the OAR. In this context, the zeroth-order transmission, defined as the fraction of incident power propagating on-axis after the filter, is $c_0^4 = (L/p)^4 = \mathrm{OAR}^2$.

Since the transmission through the filter already accounts for one factor OAR, the second OAR factor represents the fraction of transmitted light in the zeroth order, while the complementary fraction $1 - \mathrm{OAR}$ is redistributed into the higher diffraction orders. The model provides quantitative predictions for the zeroth-order and total transmission as a function of OAR and lattice geometry, which are compared against experimental measurements in Section 3.

2.3. Short-wavelength transmission measurements

The experimental setup consisted of a laser system and a vacuum chamber that houses the HHG source, IR filtering elements, focusing optics, and XUV-sensitive detectors. An overview of the setup is provided in Fig. 2(a). Short-wavelength transmission measurements were performed using a High-Harmonic Generation (HHG) source, covering the 8 − 19 nm wavelength range. The harmonics were generated using a mode-locked laser, with a central wavelength of 1030 nm giving 0.6 mJ pulses at 42 kHz for an average power of 25.2 W. The pulses were compressed to <35 fs exploiting spectral broadening and mirrors for dispersion compensation in a multi-pass cell configuration. The experiments were conducted under high-vacuum conditions, where the XUV light was generated focusing the beam on a Neon gas jet. The 6 different MPFs were installed on a motorized wheel approximately 20 cm after the gas jet, perpendicular to the incident radiation. The wheel hosted one empty slot to reference the measurement to the case without MPF. The MPF stage was followed by a 600 nm thick Zirconium filter. The radiation transmitted by the filtering apparatus was focused using a toroidal mirror onto a camera.

The data processing procedure consisted of dark-frame subtraction and background removal and a denoising step based on wavelet thresholding, using the Symlets wavelet family, to suppress high-frequency noise components.

The MPF transmission in the XUV domain was obtained integrating the full diffraction pattern, shown in Fig. 2(b-c) and normalized to the XUV signal without MPF. The zeroth order transmission was similarly computed, selecting only the central portion of the diffraction pattern.

The setup is designed for moving the toroidal mirror out of the beam path and to propagate the beam towards a XUV spectrometer composed of a Silicon transmission grating and a camera. This configuration allows the acquisition of the XUV spectrum Fig 2(d).

2.4. Infrared transmission measurements

The behavior of the MPFs in the IR domain was assessed through transmission measurements performed in a setup that closely mimics the HHG experimental setup shown in Fig. 2. The source was a Ti:Sapphire laser system at 800 nm, 40 fs pulse duration, from which 0.6 mJ pulses are used for this experiment after passing through a power regulator composed of a zero-order half-wave plate and a set of two thin film polarizers. To avoid nonlinear effects and plasma formation in air, the laser compressor was detuned to stretch the time duration of the pulses. This adjustment does not affect the measured transmission ratios. We characterized the MPF transmission at three different laser powers using a digital power-meter (ThorLabs, PM100D3), employing two different probes for each power range. We measured the total MPF transmission by collecting the full diffraction pattern and the zeroth-order transmission by spatially isolating the central diffraction peak with an aperture. All measurements were normalized to a reference acquired without the MPF in the beam path.

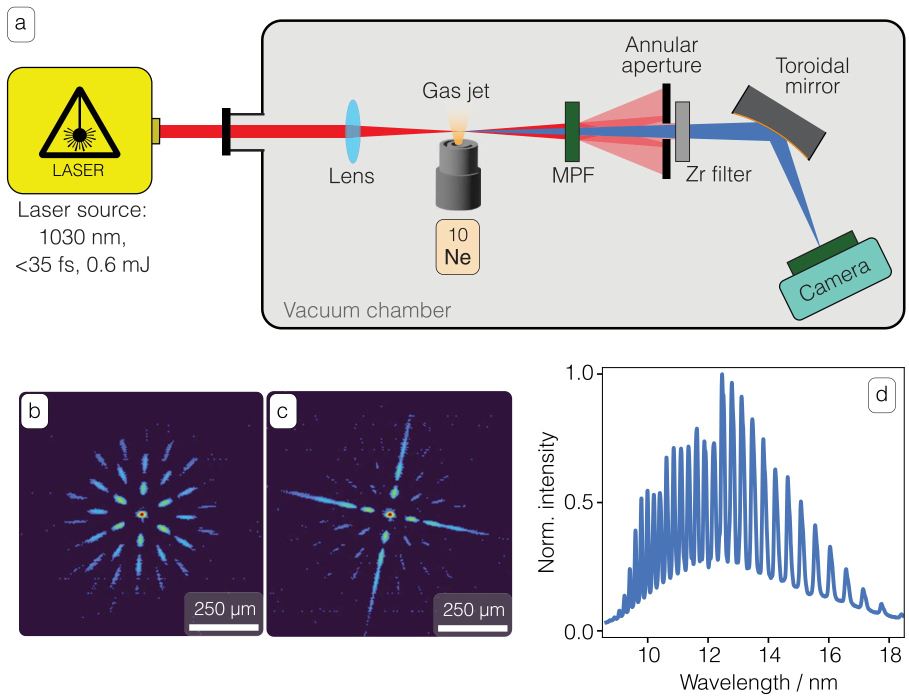

Fig. 2. (a) Schematic representation of the High-Harmonic Generation (HHG) experimental setup used for the characterization in the Soft-X Ray range. (b) In focus diffraction patterned imaged by the toroidal mirror for microporous filters with honeycomb geometry. (c) In focus diffraction patterned imaged by the toroidal mirror for microporous filters with square geometry. (d) HHG spectrum measured with a transmission grating.

3. Results and discussion

3.1. Infrared rejection

The IR rejection performance of the six MPFs was assessed at 800 nm by measuring total transmission and zeroth-order transmission, both normalized to the input power, and comparing the results against the analytical diffraction model introduced in Section 2.2. The results are summarized in Fig. 3.

We observe that the measured total IR transmission is consistently below the prediction across all samples and both geometries, with values ranging from 15.4% to 62.2% for OARs between 25% and 67%. The two geometries perform comparably at equivalent OAR, with differences falling within the measurement uncertainty, below 0.7%.

Similarly, the zeroth-order transmission of the infrared pulses is comparable for the two lattice geometries. For the lowest OAR samples ($\approx$ 25%), the zeroth-order transmission reaches 1.1%, corresponding to a suppression of approximately 99% of the incident IR power along the optical axis. Even for the highest OAR samples ($\approx$ 67%), the zeroth-order transmission does not exceed 28%, representing a suppression of more than 70%. The measured zeroth-order values fall consistently below both the model prediction and the values expected from the measured total transmission alone, indicating that the MPF achieves stronger on-axis IR rejection than the lossless model anticipates. This is a favorable outcome for the intended application. The systematic deviation from the lossless model is consistent with the breakdown of the thin-grating approximation in the IR. The thin-grating approximation holds only when in-channel diffraction

Optics EXPRESS

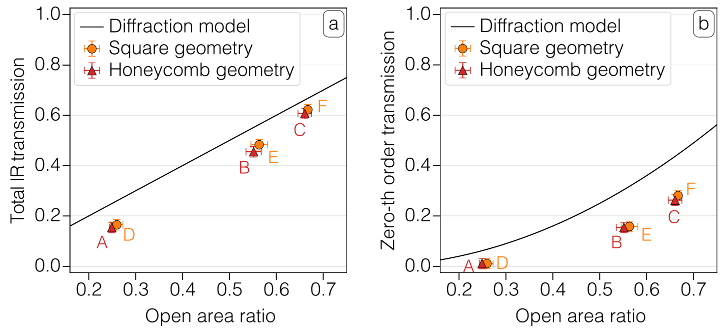

Fig. 3. Infrared rejection results at 800 nm for six MPFs with square and honeycomb geometries. (a) Total transmission and (b) zeroth-order transmission, both normalized to the incident power, as a function of OAR. Markers correspond to experimental data and error bars represent the 3-σ uncertainty. The solid lines show the prediction of the analytical diffraction model.

is weak, a condition quantified by the Fresnel number:

$$N_F = \frac{a^2}{\lambda\, d} \tag{8}$$

where a is the aperture half-width and d the channel depth. For $N_F \gg 1$ the channel transmits the input field in a ray-like manner, and the thin binary grating model applies [28,29]. On the other hand, for $N_F \sim 1$ in-channel diffraction becomes significant. With our geometries, N_F is of order 10^2 for wavelengths in the XUV range and of order unity in the IR range. This suggests that the IR field diffracts appreciably while traversing the 10 μm long channel, and a fraction of it is absorbed by the sidewalls. The same mechanism is negligible for XUV radiation. This wall interaction acts as a virtually reduced OAR and explains the discrepancy between measurements and the model for both total transmission and on-axis suppression.

The IR rejection measurements were performed at 800 nm, whereas the short-wavelength characterization and the damage tests employed a 1030 nm driver, as the two campaigns were carried out on different laser systems according to availability. The Fresnel-number framework allows the consequences of this difference to be assessed quantitatively. Since $N_F \propto 1/\lambda$, changing the wavelength from 800 nm to 1030 nm multiplies N_F by a factor of 0.78 for every device, from the range $1.4 - 4.1$ spanned by the six MPFs at 800 nm to $1.1 - 3.2$ at 1030 nm. The two intervals largely overlap and remain significantly smaller than N_F for the XUV wavelengths. The present measurements therefore already probe the regime relevant at 1030 nm, and no qualitative change in behavior is expected.

Within this picture, the deviation from the thin-grating model should, if anything, become more pronounced at 1030 nm: a lower Fresnel number implies stronger in-channel diffraction and a larger fraction of the field interacting with the channel sidewalls, both of which remove power from the zeroth order. The on-axis suppression reported here can thus be regarded as a conservative estimate of the performance at 1030 nm. The same conclusion follows from the diffraction angles, which scale with λ and are larger at 1030 nm, placing the diffracted orders further from the optical axis.

A quantitative transfer of the total transmission, however, requires more care, as the absorption of the substrate material is different at the two wavelengths. Generally, this does not affect the on-axis rejection, since the diffracting orders leave the zeroth order direction irrespective of whether they are subsequently absorbed.

3.2. Short-wavelength transmission

MPF transmission performance in the XUV domain was characterized using two complementary measurements. As explained in Section 2.3, a grating-based spectrometer and a camera placed in the focal plane were used to assess the spectral and spatial properties of the XUV beam transmitted through the MPFs.

The spectral transmission curves, shown in Fig. 4(a), were normalized to a reference acquired without any diffractive filter in the beam path. All six MPFs exhibit a flat transmission across the 8 − 19 nm spectral range, with no evidence of absorption edges or resonance features attributable to the microstructure, the silicon membrane, or the metallic coating. This confirms that MPFs operate as spectrally neutral filters in the XUV domain, consistent with the wavelength-independent efficiency prediction of the diffraction model, and validates their suitability for broadband applications, including attosecond spectroscopy and XUV reflectometry.

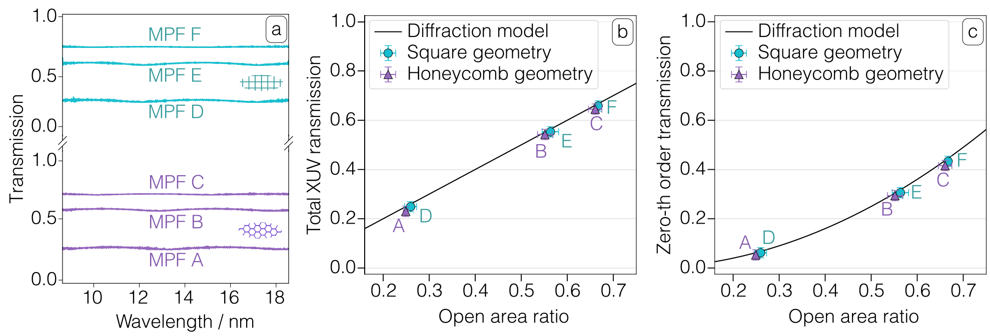

Fig. 4. Short-wavelength transmission results in the Soft-X Ray range, from 8 to 19 nm. (a) Spectral transmission of the six MPFs, normalized to the reference spectrum acquired without MPF. (b) Total MPF transmission and (c) zeroth-order XUV transmission as a function of OAR for square and honeycomb geometries. Markers correspond to experimental data; the solid line shows the OAR^2 prediction of the analytical model. The markers correspond to experimental data and error bars represent the 3-σ uncertainty.

The total transmission of the MPFs is shown in Fig. 4(b) as a function of OAR. The measured values range from 21.3% to 64.9% and show good agreement with the analytical model prediction of OAR^2, in contrast to the IR case where systematic deviations were observed. Similarly, the zeroth order transmission shows good agreement with the model prediction as reported in Fig. 4(c). In this case, the zeroth order transmission range between 5%, for the smallest OAR, and 43% for the largest OAR. The diffracted XUV orders are fully transmitted and angularly separated, and this light is not lost and remains potentially usable. For applications such as spectroscopy and scatterometry, a pinhole can be used to isolate the zeroth order alone, which preserves the properties of a gaussian beam. In other cases, however, the full diffraction pattern can be exploited for illumination. An example can be found in ptychography, where a structured probe can improve the robustness of the reconstruction and the achievable resolution [30].

3.3. Filtering performance and implications for power scaling

The complementary IR and XUV measurements allow a direct evaluation of MPF performance in the context of the power-scaling challenge for HHG beamlines. The central figure of merit is the degree to which an MPF placed upstream of a metallic filter reduces the IR power incident on the latter, while preserving the XUV flux delivered downstream.

For each MPF, the on-axis IR suppression reduces the thermal load on the downstream metallic filter by a factor equal to the zeroth-order IR transmission. In the most favorable case (≈ 25%

Optics EXPRESS

OAR), the zeroth-order IR transmission reaches 1.1%, compared to the total XUV transmission of approximately 23%.

Taking the metallic filter damage threshold as the limiting factor for system operation, the reduction in on-axis IR power at the metallic filter translates directly into a gain in the maximum driving laser power that the beamline can accommodate. Since the XUV flux scales with driving laser power, this gain propagates into a corresponding increase in achievable XUV output. In this picture, the figures of merit are the Spectral Purity (SP) and Spectral Purity Gain (SPG), defined as:

$$SP = \left.\frac{XUV}{IR}\right|_{z=MF} \qquad SPG = \frac{SP_{MPF}}{SP_{no\,MPF}} \tag{9}$$

which correspond to the XUV-to-IR power ratio at the metallic filter (MF). The SPG of the six MPFs tested in this work are shown in Fig. 5, where the SPG is the SP using an MPF, normalized to the SP in the absence of an MPF.

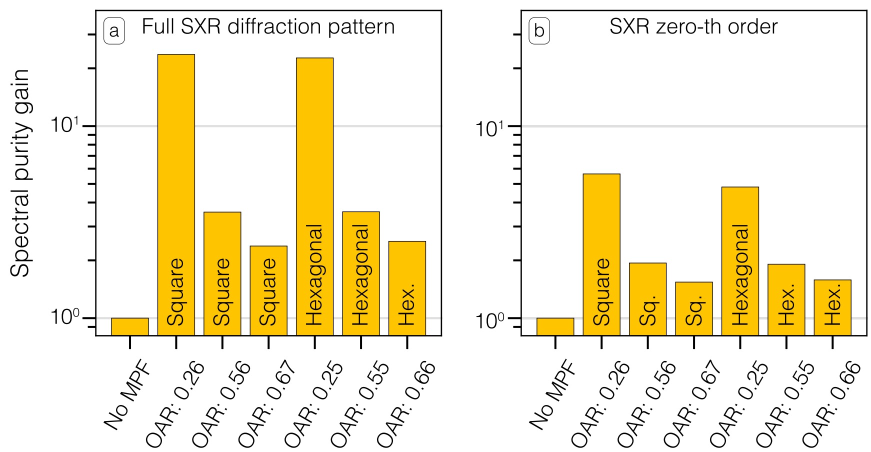

Fig. 5. Spectral purity gain (SPG) for different the MPF geometries, normalized to the SPG in the absence of an MPF. (a) SPG computed considering the full XUV diffraction pattern is collected. (b) SPG computed condidering only the on-axis XUV (zeroth-order).

We consider two different cases. Figure 5 (a) shows the SPG computed using the full XUV diffraction pattern (total XUV transmission) relative to the zeroth-order IR transmission. This represents the most favorable scenario, applicable when the entire transmitted XUV beam, including off-axis diffracted orders, can be collected and used. In this context, the SPG clearly indicates a gain exceeding one order of magnitude achieved for the lowest OAR devices. Figure 5 (b) shows the SPG in the more common experimental case, which considers only the light propagating along the optical axis, thus only the XUV zeroth-order and the IR zeroth-order transmission. This is the more conservative and experimentally relevant estimate, but it still yields substantial gains across all MPFs, confirming that the improvement in spectral purity is robust regardless of whether the full diffraction pattern or only the zeroth-order XUV beam is exploited.

The trade-off between IR suppression and XUV transmission is governed by the OAR, as lower OAR provides stronger IR rejection at the cost of reduced XUV throughput, while higher OAR preserves more XUV flux but offers less IR suppression. The optimal OAR for a given application will depend on the relative weights assigned to XUV flux and metallic filter lifetime. These results highlight the potential of MPFs to meaningfully extend the operating range of compact HHG sources toward kilowatt-class driving lasers, where conventional metallic filter configurations are currently among the limiting components.

Optics EXPRESS

3.4. Damage threshold

The structural robustness of the MPFs under IR irradiation was assessed to verify the maximum average intensity conditions that MPFs can withstand. In this context, the average intensity is defined as the ratio between the impinging average power and the illumination area. The tests were performed using a 1030 nm laser source delivering ∼ 500 ps pulses at 42 kHz [31]. The system was equipped with a power regulator to sweep the 3 to 300 W average power range. The front-end output beam used had an elliptical cross-section profile, with a Gaussian intensity profile along both directions, and with a total $1/e^2$ area of 0.105 cm^2 on the test plane where the filters were collocated. Structural integrity was inspected by optical microscopy and Scanning Electron Microscopy (SEM) after each exposure to the laser beam. The zeroth-order transmission was monitored as a function of exposure time to detect performance degradation in situ. All the damage tests were performed in air conditions at ambient pressure. The results are shown in Fig. 6.

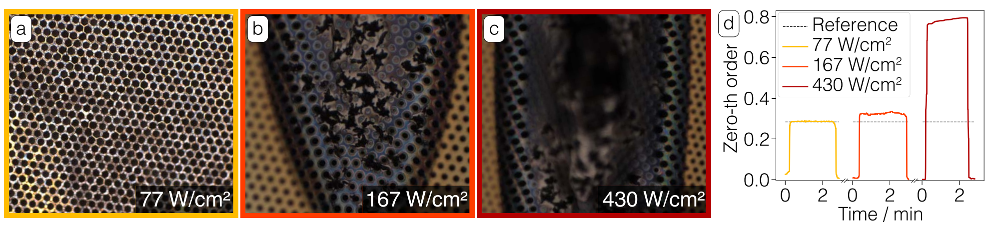

Fig. 6. Microporous filter damage threshold characterization at 1030 nm. (a), (b) and (c) Optical microscopy images of the MPF surface after exposure at the indicated average intensity levels, showing the progression of structural damage upon the increasing power load. (d) Zeroth order transmission as a function of exposure time at the average intensities connected to panels a-c.

The damage assessment revealed slight damage to the metallic coating of the MPFs for impinging average intensities around 75 W/cm^2, as shown in Fig. 6 (a). This instance did not cause an alteration to the diffraction pattern or the MPF filtering properties. The zeroth-order transmission remained stable at all tested intensities up to approximately 160 W/cm^2, around which slight structural damage was observed (Fig. 6(b)), accompanied by the onset of transmission degradation. At 400 W/cm^2, the IR filtering capability of the MPF was fully compromised (Fig. 6(c)), with the zeroth-order transmission approaching the unfiltered value, as shown in Fig. 6(d). The damage tests were repeated on MPFs with different open-area ratios, and no significant difference in the damage onset was observed within the resolution of the intensity steps employed.

These tests characterize the average-power and thermal damage threshold of the devices rather than a single-pulse ablation threshold. The fluence at the damage onset of 3.8 mJ/cm^2 lies nearly two orders of magnitude below the ablation threshold of crystalline silicon, which is 200 mJ/cm^2 and remains nearly constant for $5 - 400$ fs pulse durations [32]. A dedicated characterization of the damage threshold in the femtosecond regime, nevertheless, remains desirable and is beyond the scope of this work.

Under identical experimental conditions, we tested the damage threshold of conventional metallic filters, Zr and Al, all with a thickness of approximately 200 nm with an aperture of 15 mm and the membrane was supported by a Ni mesh. The filters exhibited complete structural failure at approximately 7 W/cm^2, which is more than one order of magnitude below the MPF damage onset. This comparison directly quantifies the improvement in robustness against power loads that MPFs offer over the current standard approach.

The superior damage threshold of the MPFs is consistent with their operating principle: rather than only reflecting and absorbing the IR radiation, the array of hollow channels redirects it into off-axis diffraction orders, substantially reducing the heat deposited in the device. The residual thermal load, and consequently the onset of structural damage, is therefore determined by the fraction of IR power that is absorbed by the silicon membrane and its metallic coating rather than diffracted away. In this context, the metallic coating serves a dual purpose: it reflects impinging IR radiation before it can be absorbed by the underlying Silicon, and enhances the thermal conductivity of the structure, facilitating heat dissipation. Optimization of the coating thickness and material may therefore offer a route to further increase the damage threshold, for example by implementing a protected Ag coating with higher IR reflectivity.

4. Conclusions

We have demonstrated microporous filters as transmissive diffractive elements for IR suppression in HHG beamlines, and characterized their performance across the IR and XUV spectral domains. Six MPFs with square and honeycomb lattice geometries and open-area ratios between 25% and 67% were fabricated on silicon-on-insulator wafers and systematically evaluated against an analytical scalar diffraction model.

In the IR domain, all MPFs exhibit effective on-axis suppression, with zeroth-order transmission as low as 1.1% for the lowest OAR samples, corresponding to a rejection of approximately 99% of the incident power along the optical axis. The measured suppression consistently exceeds the model prediction, and the two lattice geometries perform comparably at equivalent OAR, confirming that the suppression mechanism is governed primarily by the open-area ratio rather than the specific channel arrangement.

In the XUV domain, MPFs transmit broadband radiation in the 8 to 19 nm spectral range without introducing spectral distortion. The zeroth-order XUV transmission closely follows the OAR^2 model prediction, and the full diffracted pattern remains accessible for applications where off-axis light can be collected.

This work also reports thermal damage tests, showing that MPFs withstand average intensities up to approximately 160 W/cm^2 without degradation of their filtering properties, and retain partial functionality up to 400 W/cm^2. This represents an improvement of more than one order of magnitude over conventional metallic filters.

The spectral purity gain analysis confirms the performance impact of MPFs on HHG beamlines in terms of gains that exceed one order of magnitude in the XUV-to-IR power ratio at the downstream metallic filter for the lowest OAR devices. This gain translates directly into an extension of the maximum driving laser power that the beamline can accommodate before metallic filter damage, and consequently into higher achievable XUV output. The OAR provides a continuous and predictable parameter for trading off IR suppression against XUV throughput, enabling straightforward optimization for a given source and application.

These results establish MPFs as a viable and robust component for IR management to keep the power-scaling pace of HHG sources up. Future work may explore sub-wavelength pitch designs for enhanced IR rejection via Faraday cage insulation, alongside alternative coatings and hyperuniform disordered geometries for engineered angular redistribution of the rejected IR power.

Funding. Dutch Research Council (VI.Vidi223.133, OTP grant no. 18703); HORIZON EUROPE European Research Council (101041819).

Acknowledgment. We acknowledge MICROCREATE B.V. for the mircofacbrication service. We thank J. Reinink for the help in the preparation and execution of part of the experiments reported in this work.

This work was conducted at the Advanced Research Center for Nanolithography, a public-private partnership between the University of Amsterdam (UVA), Vrije Universiteit Amsterdam (VU), Rijksuniversiteit Groningen (RUG), the Netherlands Organization for Scientific Research (NWO), and the semiconductor equipment manufacturer ASML and was

Optics EXPRESS

(partly) financed by "Toeslag voor topconsortia voor kennis en innovatie (TKI)" from the Dutch Ministry of Economic Affairs and Climate Policy.

This manuscript is part of a project that has received funding from Open Technologieprogramma (OTP) by NWO, grant no. 18703. It also got support from the European Research Council (ERC) under the European Union's Horizon Europe research and innovation programme (grant agreement no. 101041819, ERC Starting Grant ANACONDA) as well as the Vidi research programme HIMALAYA with project number vi.vidi.223.133 financed by NWO.

Disclosures. The authors declare no conflicts of interest.

Data availability. Data underlying the results presented in this paper are not publicly available at this time but may be obtained from the authors upon reasonable request.

References

1. A. Rundquist, C. G. Durfee III, Z. Chang, *et al.*, "Phase-matched generation of coherent soft x-rays," Science **280**(5368), 1412–1415 (1998).
2. T. Popmintchev, M.-C. Chen, D. Popmintchev, *et al.*, "Bright coherent ultrahigh harmonics in the kev x-ray regime from mid-infrared femtosecond lasers," Science **336**(6086), 1287–1291 (2012).
3. F. Krausz and M. Ivanov, "Attosecond physics," Rev. Mod. Phys. **81**(1), 163–234 (2009).
4. P. M. Kraus, M. Zürch, S. K. Cushing, *et al.*, "The ultrafast x-ray spectroscopic revolution in chemical dynamics," Nat. Rev. Chem. **2**(6), 82–94 (2018).
5. C. Porter, T. Coenen, N. Geypen, *et al.*, "Soft x-ray: novel metrology for 3d profilometry and device pitch overlay," in *Metrology, Inspection, and Process Control XXXVII*, vol 12496, (SPIE, 2023), pp. 412–420.
6. F. Corazza, E. Kechaoglou, L. Guery, *et al.*, "Broadband extreme ultraviolet zeroth order scatterometry for nanostructure metrology," Nat. Commun. **17**(1), 6573 (2026).
7. R. Klas, A. Kirsche, M. Gebhardt, *et al.*, "Ultra-short-pulse high-average-power megahertz-repetition-rate coherent extreme-ultraviolet light source," PhotoniX **2**(1), 4 (2021).
8. S. Hädrich, J. Rothhardt, M. Krebs, *et al.*, "Single-pass high harmonic generation at high repetition rate and photon flux," J. Phys. B: At., Mol. Opt. Phys. **49**(17), 172002 (2016).
9. R. Weissenbilder, S. Carlström, L. Rego, *et al.*, "How to optimize high-order harmonic generation in gases," Nat. Rev. Phys. **4**(11), 713–722 (2022).
10. J. Rothhardt, S. Hädrich, A. Klenke, *et al.*, "53 w average power few-cycle fiber laser system generating soft x rays up to the water window," Opt. Lett. **39**(17), 5224–5227 (2014).
11. P. W. Vedder and J. F. Lindblom, "Thin film filter performance for extreme ultraviolet and x-ray applications," Opt. Eng. **29**(6), 614–624 (1990).
12. E. J. Takahashi, H. Hasegawa, Y. Nabekawa, *et al.*, "High-throughput, high-damage-threshold broadband beam splitter for high-order harmonics in the extreme-ultraviolet region," Opt. Lett. **29**(5), 507–509 (2004).
13. O. Pronin, V. Pervak, E. Fill, *et al.*, "Ultrabroadband efficient intracavity xuv output coupler," Opt. Express **19**(11), 10232–10240 (2011).
14. S. Andreev, A. Akhsakhalyan, M. Bibishkin, *et al.*, "Multilayer optics for xuv spectral region: technology fabrication and applications," Cent. Eur. J. Phys. **1**, 191–209 (2003).
15. M. Trost, S. Schröder, A. Duparré, *et al.*, "Structured mo/si multilayers for ir-suppression in laser-produced euv light sources," Opt. Express **21**(23), 27852–27864 (2013).
16. L. Poletto and F. Frassetto, "Time-preserving grating monochromators for ultrafast extreme-ultraviolet pulses," Appl. Opt. **49**(28), 5465–5473 (2010).
17. F. Frassetto, P. Villoresi, and L. Poletto, "Beam separator for high-order harmonic radiation in the 3-10 nm spectral region," J. Opt. Soc. Am. A **25**(5), 1104–1114 (2008).
18. J. Peatross, J. Chaloupka, and D. Meyerhofer, "High-order harmonic generation with an annular laser beam," Opt. Lett. **19**(13), 942–944 (1994).
19. R. Klas, A. Kirsche, M. Tschernajew, *et al.*, "Annular beam driven high harmonic generation for high flux coherent xuv and soft x-ray radiation," Opt. Express **26**(15), 19318–19327 (2018).
20. C. Jin, X. Tang, B. Li, *et al.*, "Optimal spatial separation of high-order harmonics from infrared driving lasers with an annular beam in the overdriven regime," Phys. Rev. Appl. **14**(1), 014057 (2020).
21. H. Schnopper, L. Van Speybroeck, J. Delvaille, *et al.*, "Diffraction grating transmission efficiencies for xuv and soft x rays," Appl. Opt. **16**(4), 1088–1091 (1977).
22. Y. Suzuki, K. Totsu, M. Moriyama, *et al.*, "Free-standing subwavelength grid infrared cut filter of 90 mm diameter for lpp euv light source," Sens. Actuators, A **231**, 59–64 (2015).
23. K. Jefimovs, J. Laukkanen, T. Vallius, *et al.*, "Free-standing inductive grid filter for infrared radiation rejection," Microelectron. Eng. **83**(4-9), 1339–1342 (2006).
24. Q. Zhang, K. Zhao, J. Li, *et al.*, "Suppression of driving laser in high harmonic generation with a microchannel plate," Opt. Lett. **39**(12), 3670–3673 (2014).
25. Z. Cao, F. Jin, J. Dong, *et al.*, "Soft x-ray low-pass filter with a square-pore microchannel plate," Opt. Lett. **38**(9), 1509–1511 (2013).
26. F. Laermer and A. Urban, "Mems at bosch–si plasma etch success story, history, applications, and products," Plasma Processes Polym. **16**(9), 1800207 (2019).

27. B. Wu, A. Kumar, and S. Pamarthy, "High aspect ratio silicon etch: A review," J. Appl. Phys. **108**(5), 051101 (2010).
28. J. W. Goodman, *Introduction to Fourier Optics* (W. H. Freeman, 2017), 4th ed.
29. A. García-Sánchez and Á. S. Sanz, "Analysis of the gradual transition from the near to the far field in single-slit diffraction," Phys. Scr. **97**(5), 055507 (2022).
30. A. Pelekanidis, F. Zhang, M. Gouder, *et al.*, "Illumination diversity in multiwavelength extreme ultraviolet ptychography," Photonics Res. **12**(12), 2757–2771 (2024).
31. J. H. Buss, S. Starosielec, M. Schulz, *et al.*, "Mid-infrared optical parametric chirped-pulse amplifier at 50 w and 38 fs pumped by a high-power yb-innoslab platform," Opt. Express **32**(21), 36185–36192 (2024).
32. J. Bonse, S. Baudach, J. Krüger, *et al.*, "Femtosecond laser ablation of silicon–modification thresholds and morphology," Appl. Phys. A **74**(1), 19–25 (2002).